Journal of Materials Science: Materials in Electronics (2020) 31:13756–13764
https://doi.org/10.1007/s10854-020-03935-1

Comparison of optoelectronic properties of epitaxial and non-epitaxial GaN nanostructures

Kishor Upadhyaya[1] · **Narasimha Ayachit**[1] · **S. M. Shivaprasad**[2]

Received: 5 April 2020 / Accepted: 3 July 2020 / Published online: 10 July 2020

Abstract
Structural, optical and surface properties of epitaxially grown 2D GaN nanowall network using Molecular Beam Epitaxy have been compared to those of non-epitaxially grown single-crystalline 1D GaN nanowires using Chemical Vapour Deposition. The kinetics of growth mechanisms and formed morphology are shown to significantly influence the respective band structures and consequently their luminescence properties. X-ray diffraction and Raman spectroscopy reveal that the epitaxial 2D nanowall network experiences a hydrostatic strain in addition to a compressive strain, whereas non-epitaxial 1D nanowires possess a morphology-dependent tensile/compressive strain and a negligible hydrostatic strain. Slightly blue-shifted photoluminescence emission from both these nanostructures is markedly enhanced compared to that from an epilayer. The epitaxial nanowall network exhibits the highest enhancement in the band edge emission among them. X-ray photoelectron spectroscopy spectra show shifts in the valence band features and in the hybridization of shallow core levels. Using the XRD, Raman, PL and XPS data, a variation in the band structure of these differently kinetically formed GaN nanostructures is also sketched.

1 Introduction

Appropriately self-assembled low-dimensional materials exhibit size-dependent properties and hence have opened new vistas of technology that were not conceivable before. The last two decades have seen intense research activity in the field of low-dimensional materials, which is of both phenomenological and technological importance, to understand and harvest this novel knowledge for useful applications. Especially, low-dimensional semiconductor materials have become an integral part of a wide range of modern optoelectronic devices such as light-emitting diodes, lasers, photo detectors, field emitters, high electron mobility transistors, field effect transistors, biochemical sensors, short wavelength communication (5G onwards), data storage and processing, and bio-imaging. Many nitride semiconductors like g-C_3N_4, BN and TiN have been studied extensively in the past couple of decades to explore their suitability for photocatalysis, coating applications, etc. [1–4]. After blue light emission was demonstrated by Nakamura et al. in 1990s, GaN has been one of the most studied semiconductor materials in recent past, due to its wide direct bandgap (3.4 eV), high temperature and power sustainability, mobility, melting point, low electron affinity (2.7–3.3 eV) and chemical stability which make it desirable for the range of applications mentioned earlier [5–11]. Forming self-assemblies of GaN of various nano-manifestations such as pyramids, rings, belts, wires, rods, walls and irradiated flat surfaces are being probed intensively to not only observe tunable characteristic properties unprecedented that were not possible in their bulk forms [12–17]. The role of strain, point and extended defects, assembly of nanostructures, etc. have become crucial in translating these basic information into usable optoelectronic devices.

Nanostructured GaN thin films can be grown using different growth techniques such as vapour phase epitaxy (VPE), molecular beam epitaxy (MBE) and chemical vapour deposition (CVD) which employ different growth routes that influence the crystallization process and defect density, which in turn influences the optical properties [18–22]. In epitaxial techniques like MBE, the lattice mismatch between the substrate and the GaN overlayer influences the crystal structure, strain, dislocation density, defects, etc. and hence by controlling the growth kinetics, different nanostructured

✉ Kishor Upadhyaya
kishor@kletech.ac.in

[1] Thin Films Lab, Centre for Materials Science, K.L.E Technological University, Hubballi 580031, India

[2] International Centre for Materials Science, Jawaharlal Nehru Centre for Advanced Scientific Research, Bangalore 560064, India

morphologies are obtained. In non-epitaxial techniques like CVD, an assembly of metal catalyst nanoparticles are used on the substrate to initiate the growth. The choice of catalyst and temperature majorly influence the emerging structural properties while the growth proceeds via vapour–liquid–solid (VLS) mechanism. Several efforts to tune the properties of GaN by employing various growth techniques have been reported in the literature [23–31], but a precise control of the assembly of these structures for gainful applications is still elusive.

In this work, we have compared two different single-crystalline morphologies, viz. epitaxial 2D Nanowall Network (NWN) grown by Molecular Beam Epitaxy (MBE) on sapphire and non-epitaxial 1D Nanowires (NW) grown by Chemical Vapour Deposition (CVD), respectively. The role of growth mechanism on the morphology and crystallinity of the nanostructures has been elucidated, and morphology and their role in the enhancement of luminescence properties have been reported.

2 Experimental procedure

GaN thin films were grown using both Low Pressure Chemical Vapour Deposition (CVD) and Molecular Beam Epitaxy (MBE) to obtain nanostructures with different morphologies. Films grown on CVD (custom built) used chemically cleaned Si(111) as substrate on which 2-nm-thick Au (99.99% wire from Alfa Aesar) was deposited by e-beam evaporation with a beam current of 5nA and base pressure of 1.0×10^{-9} Torr. A Quartz Crystal Microbalance was used to monitor the coverage of Au deposited on the substrate. This substrate was then placed at a distance of 10 mm from Ga metal (99.99%, Alfa Aesar) in an alumina crucible and introduced in a horizontal tubular furnace with a base pressure of 10^{-3} mbar. Growth was carried out for 2 h with ammonia flow rate of 200 sccm at 800 °C and 850 °C to obtain nanorods (NR) and nanowires (NW), respectively. The reactor was turned off after the growth to naturally cool down to room temperature. Similarly, epitaxial films were grown using MBE (SVT associates, USA) on chemically cleaned Al_2O_3 (0001) which was degassed at 500 °C in 1×10^{-9} Torr vacuum inside the preparation chamber for 60 min, and again degassed at 800 °C in 3×10^{-11} Torr inside the growth chamber for 30 min. Growth of GaN films was carried out under optimized nitrogen-rich conditions (III–V ratio 1:100) at a base pressure of 3×10^{-11} Torr, at substrate temperatures of 630 °C and 680 °C and growth durations of 3 h and 4 h to obtain the blunt and sharp tipped nanowall network (NWN) morphologies. In both the cases, 4.5 sccm N_2 gas flow rate with a RF forward power of 375 W was maintained while Ga Knudsen cell was kept at 1000 °C.

Field Emission Scanning Electron Microscope (FESEM) (Quanta 3D FEG, FEI, Netherlands) images were captured at an operating voltage of 10–30 kV and different magnifications. Imagej software was used to perform image analysis to obtain size distribution, surface area, etc. X-ray diffraction (XRD) (Brüker, USA) with a Cu Kα source (1.5406 Å) was used to study the crystal structure of the films. Photoluminescence (PL) (Horiba JobinYvon, Japan) spectrophotometer with 325 nm excitation wavelength from a Xe lamp with 8mW power was used to look at optical emission at room temperature. X-ray photoelectron spectroscopy (XPS) (EAC 2000 SPHERA 547 spectrometer, Omicron) studies were performed using AlKα anode (1486.7) with an X-ray spot diameter of 3–4 mm to study the electronic band structure. Calibration of binding energies was done by measuring the Fermi energy on an Ag foil in electrical contact with the sample. The spectra were acquired with a hemispherical analyser with a pass-energy of 100 eV for core-level survey scans and 25 eV for valence band scans. Shirley background correction and Gaussian line shapes were used for valence band peak fitting, and the position of the valence band maximum was obtained by linearly fitting its leading edge to the baseline. Raman spectra (inVia Renishaw, UK) were obtained in the 180° backscattering mode using Nd:YAG solid-state laser with ~ 8 mW power and 532 nm excitation with a grating monochromator (2400/1800grooves/mm) and Peltier cooled Charge Coupled Device detector. A commercially acquired GaN epilayer (TDI, USA) with 2-µm-thickness flat film grown by Vapour Phase Epitaxy method and bulk GaN powder (Alfa Aeser, Germany) was used as a reference for all the studies.

3 Results and discussion

Figure 1 shows FESEM images of GaN films of various morphologies grown by CVD (Fig. 1a, b) and PAMBE (Fig. 1c, d). 1D nanostructured GaN films grown by CVD at 800 °C (Fig. 1a) and 850 °C (Fig. 1b) contain nanorods (NR) and interconnected nanowires (NW), respectively. Image analysis reveals that the average diameter and length of NR are 140 nm and 1.37 µm (aspect ratio ≈ 10), whereas for NW these values are 15 nm and 3.54 µm (aspect ratio ≈ 236), respectively, with a 23 times larger average aspect ratio. In the VLS growth method, at a relatively lower temperature of 800 °C, the depleted availability of N-species due to slow decomposition of ammonia results in Ga-rich Au–Ga supersaturated alloy nuclei particles, which preferentially grow radially. Adatoms arriving directly onto the c-plane of the nanostructure and the sidewall diffusion cause further increase in both radial and axial directions, thereby leading to the formation of larger diameter NRs. However, higher growth temperature (850 °C) increases the ammonia

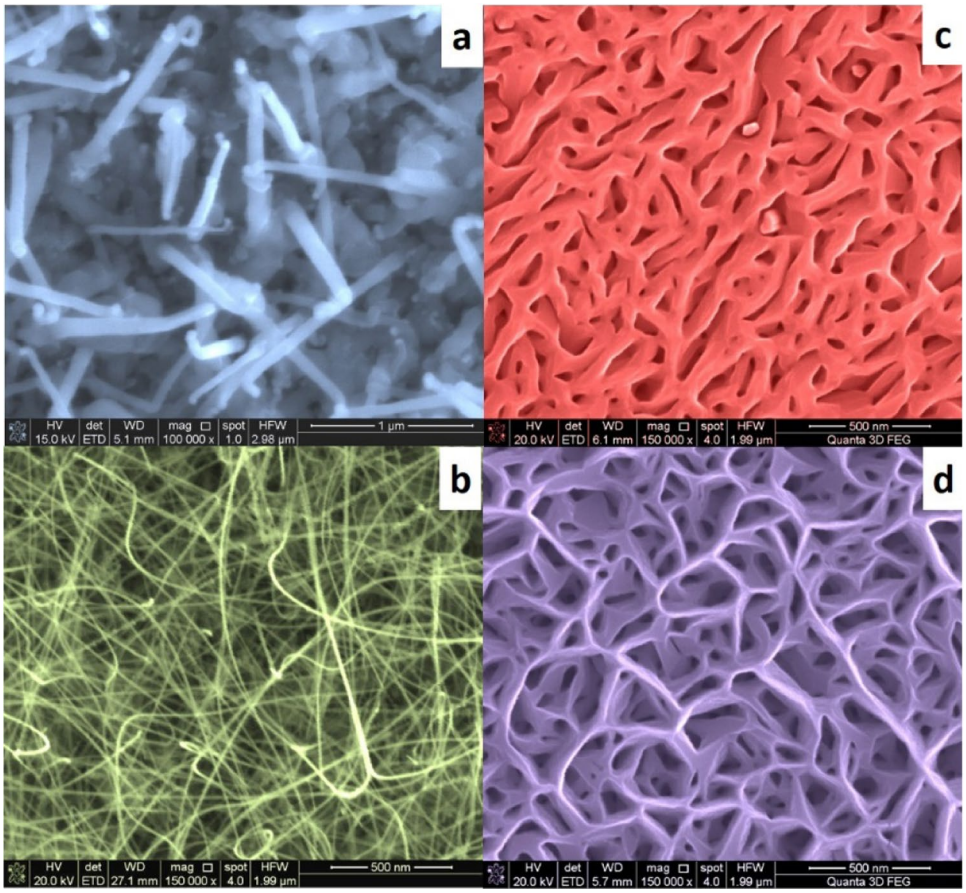

Fig. 1 FESEM plan view images of CVD-grown GaN **a** Nanorods (NR), **b** Nanowires (NW) and PAMBE grown, **c** Blunt Nanowall Network (b-NwN), **d** Sharp Nanowall Network (s-NwN)

decomposition rate and aids axial growth resulting in the formation of smaller diameter NWs. In addition, at 850 °C the Ga vapour pressure is relatively higher, and hence the growth rate is higher, leading to the growth of a continuous interconnected network long NWs [32]. Figure 1c, d shows the FESEM images of blunt tipped and sharp tipped GaN Nanowall Network (NWN) grown by MBE. These NWNs are formed by open screw dislocations as a route to relax the lattice mismatch-induced tensile stress at the interface of GaN and sapphire as described elsewhere [33]. Even though the average height (≈ 600 nm) and width at the base (≈ 160 nm) of both kinds of nanowalls are the same, the average width at the tips is 8 times narrower in the sharp Nanowall Network (s-NwN) (≈ 10 nm) compared to the blunt Nanowall Network (b-NwN) (≈ 80 nm).

Figure 2 shows the X-ray diffraction scans for GaN NW, NR, s-NwN, b-NwN and flat epilayer with peaks for GaN bulk powder (for reference) indicated by dotted lines. All the peaks can be indexed to wurtzite GaN (JCPDS card no: 898624). GaN (0002) peaks were observed at $2\theta = 34.62°$, 34.50°, 34.56° and 34.58° for NR, NW, s-NwN and b-NwN samples, respectively. Peaks were observed at 34.53° and 34.54° for bulk and epilayer samples, which shift towards higher 2θ value for NR, s-NwN and b-NwN films, indicating

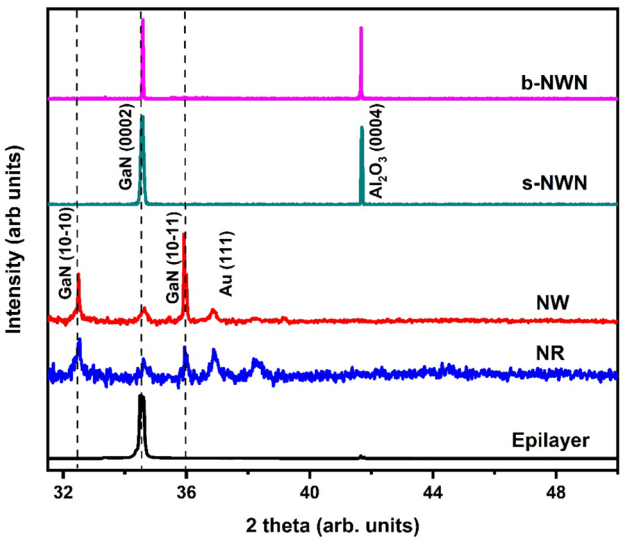

Fig. 2 X-ray diffraction 2 theta patterns for GaN thin film samples NR, NW, s-NwN, b-NwN and epilayer

the presence of a compressive strain. However, the NW peak shifts to a lower 2θ value, indicating a tensile strain in the film along c-axis. NW and NR show peaks at 32.49° and

32.50º corresponding to GaN (10–10) plane which appears at 32.25º for bulk GaN. An off-axis peak corresponding to GaN (10–11) appears at 35.85^0 and 36.00^0 for NW and NR, respectively, which arises due to the tilt of the NWs and NRs along that direction. Peaks around 31º and 37º for NR and NW correspond to the Si substrate and Au (111) catalyst, respectively. Similarly, the peak around 41º for s-NwN and b-NwN corresponds to the Al_2O_3 (0004) substrate.

Lattice parameters of all the samples (shown in Table 1) along with epilayer are calculated based on the shifts in their 2θ peak positions with respect to bulk GaN powder (stress-free) taken as reference. Stress values along both *c*- and *a*-directions are calculated using Hooke's law:

$$\sigma_{ii} = \varepsilon_{ii}\left(\frac{E}{\nu}\right), \tag{1}$$

where E is bulk modulus (200 GPa) and ν is Poisson's ratio (0.28) and ε_{ii} is the strain ($i = z$ for out of plane and $i = x$ for in plane). These values are calculated using

$$\varepsilon_c = \frac{c - c_0}{c_0} \text{ and } \varepsilon_a = \varepsilon_{xx} = \frac{a - a_o}{a_o}, \tag{2}$$

where c and a are lattice parameters of the film and c_0 and a_0 are the lattice parameters of bulk GaN (powder).

Among all the four samples studied, only NW shows larger '*c*' value than that of bulk GaN, indicating the presence of a tensile stress along *z*-axis, while other three films experience compressive stress along the same direction, as evident from their smaller '*c*' values. It is evident from Table 1 that both NR and b-NWN samples are more stressed than NW and s-NWN, which have smaller sized nanostructures. Surprisingly, the stress values of epitaxially grown 2D NWN morphologies are lesser than the 1D NWs and NRs indicating that the NWN morphology undergoes a more relaxed atomic re-arrangement during the crystallization process. Even though both s-NwN and b-NwN are epitaxially grown, the stress in s-NwN due to lattice mismatch is better relaxed by forming larger cavities compared to those in b-NwN sample. This reduces the contact area between s-NwN and c-plane sapphire at the interface leading to minimal strain on the film. However, the b-NwN that possesses smaller cavities exhibit larger strain due to lattice mismatch caused by higher contact area with the c-plane sapphire. Since, NW and NR samples are grown on Au coated Si substrate, they are not in direct contact with Si surface. NRs possess larger diameters (≈ 140 nm) than NWs (≈ 15 nm) right from the nucleation stage and possess larger stress. Both NWs and NRs exhibit biaxial strain, wherein NW has tensile strain and NR has compressive strain along *c*-direction and tensile strain along *a*-direction.

Figure 3 shows the Raman spectra acquired for all the samples along with epilayer. In the backscattering geometry A_1 (LO), E_2 high and E_2 low modes are active. E_2 (high) mode peaks which correspond to N atoms vibrating in GaN of NW, NR, b-NwN, s-NwN and epilayer are shown in Fig. 3a, and are observed to vary with in-plane stress. This peak at 566.40 cm^{-1} for bulk powder sample is taken as reference to calculate the in-plane strain values (σ_c) of all the samples, using the Kozawa relation,

$$\Delta E_2 = \sigma_c \times (4.2 \pm 0.3)\text{cm}^{-1}\,\text{GPa}^{-1}. \tag{3}$$

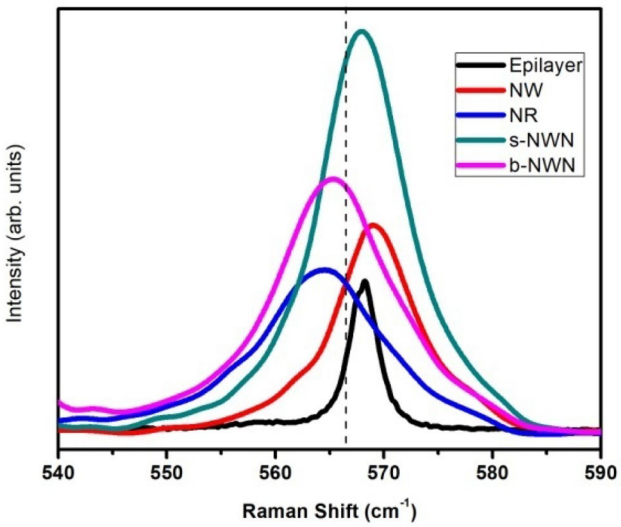

Fig. 3 Raman spectra around E_2 (high) mode of epilayer, NW, NR, s-NWN and b-NWN samples

Table 1 Lattice parameters, strain and stress values for NR, NW, s-NwN, b-NwN, epilayer and bulk (powder) samples

Sample	'*a*' (Å)	'*c*' (Å)	ε_c	ε_a	σ_c(GPa)	σ_a(GPa)	c_{13}/c_{33}
Bulk	3.1891	5.1886	–	–	–	–	–
Epilayer	3.1159	5.2345	8.85×10^{-3}	-2.29×10^{-2}	4.65	–	0.1930
NR	3.4503	5.1764	-2.35×10^{-3}	8.19×10^{-2}	−1.24	43.10	0.0142
NW	3.4627	5.1958	1.38×10^{-3}	8.58×10^{-2}	0.73	45.15	−0.0008
s-NwN	–	5.1863	-0.44×10^{-3}	–	−0.23	–	–
b-NwN	–	5.1832	-1.04×10^{-3}	–	−0.74	–	–

Table 2 Relative Raman shift with reference to peak position of E2 (high) mode of bulk powder for epilayer, NW, NR, s-NWN and b-NWN samples along with Stress values calculated from Eq. 3

Sample	E_2(high) cm^{-1}	Relative Raman shift (ΔE_2) in cm^{-1}	FWHM (eV)	Stress (σ_c) in GPa
Bulk	566.40	–	–	–
Epilayer	568.23	1.83	0.394	0.44
NW	569.03	2.63	1.147	0.63
NR	564.54	−1.86	1.841	−0.44
s-NwN	567.96	1.56	1.148	0.37
b-NwN	565.32	−1.08	1.711	−0.26

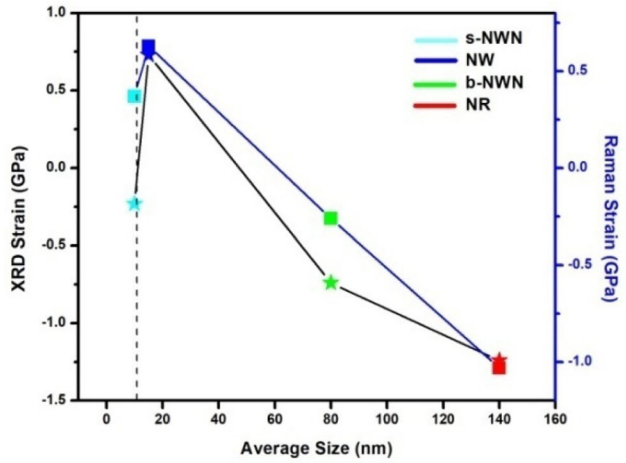

Fig. 4 Comparative plot of strain values calculated from Raman and XRD studies vs average size of the nanostructures in NW, NR, s-NWN and b-NWN. (Dotted line indicates Bohr exciton radius ≈ 11 nm)

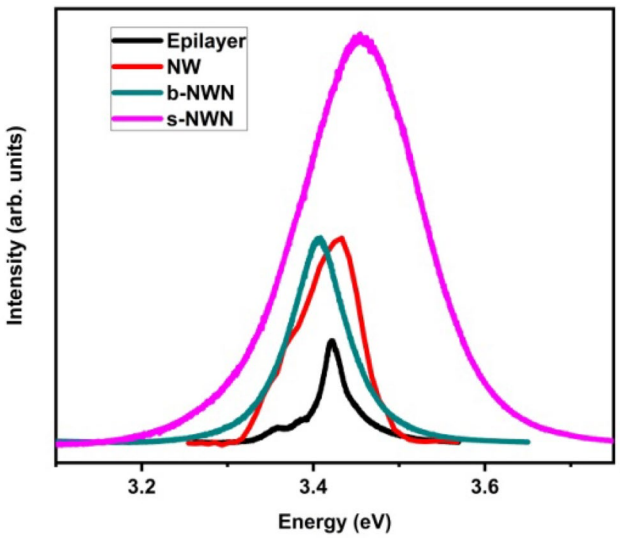

Fig. 5 Photoluminescence spectra for NW, s-NWN, b-NWN and epilayer

The relative Raman shifts for epilayer, NW and s-NWN are towards higher wavenumbers indicating the presence of a tensile stress, whereas NR and b-NWN samples exhibit shift to lower wavenumbers signifying a compressive stress on the N atoms in their respective unit cells. The values of σ_c obtained from these Raman shifts (Table 3) for NW, NR and s-NWN are within agreeable range with the values obtained from XRD measurements and (Table 1). However, in case of b-NWN the value of σ_c obtained from Raman shift is much lesser compared to that calculated from XRD measurements, indicating an out-of-plane hydrostatic stress which is not reflected as Raman shift of the E_2 (high) mode. Table 2 shows the estimated stress values along with the Raman shift for all the samples.

Figure 4 shows a plot of stress values calculated from both Raman and XRD studies vs the average size of nanostructures. As mentioned earlier, the smaller nanostructures possess lower stress compared to that in larger nanostructures, indicating that strain relaxation is higher in smaller dimensions. It is also evident that the stress values obtained from Raman and XRD studies are almost similar for CVD-grown 1D NW and NR samples but slightly different for the MBE-grown NWN samples because of internal hydrostatic stress in addition to the compressive stress.

Figure 5 shows photoluminescence spectra acquired from NW, s-NWN and b-NWN samples in comparison with that of epilayer. All the nanostructured samples possess strong enhanced Band Edge Emission (BEE) compared to that of the epilayer with varying FWHMs and peak positions. BEE from epilayer has a maximum at 3.42 eV with FWHM of 40 meV. Emission from NW and s-NWN samples exhibits a small blue shift to 3.43 eV and 3.45 eV, whereas b-NWN is red-shifted to 3.40 eV. The FWHM and intensity of the BEE peaks for all the nanostructured samples are higher due to the presence of a large number of band tail states which also contribute to the radiative recombination [34].

Figure 6 shows the valence band spectra of NW, s-NWN, b-NWN and epilayer obtained from XPS measurements which also shows shallow core levels. These spectra are deconvoluted to look at the binding energies of various hybridized levels in all the samples. For epilayer and b-NWN, the spectra are resolved into four peaks, whereas for NW and s-NWN spectra are deconvoluted into five peaks

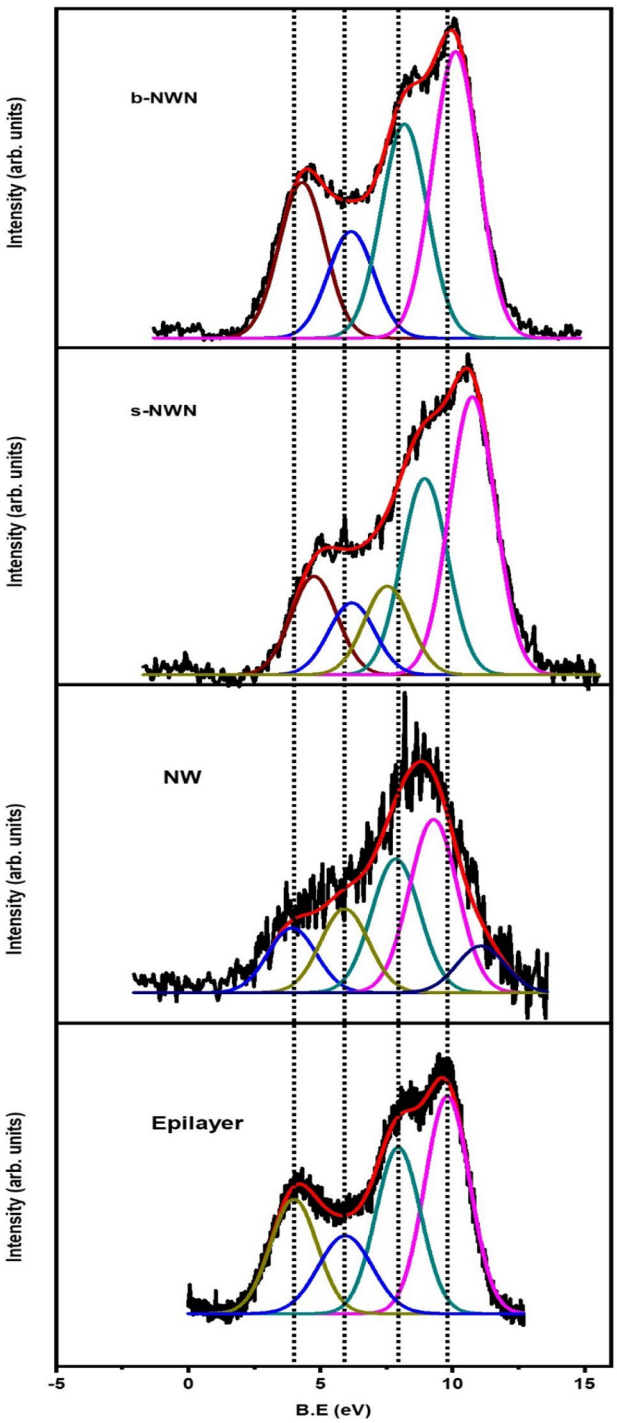

Fig. 6 Deconvoluted XPS valence band with shallow core levels spectra for NW, s-NWN, b-NWN and epilayer

each, and these values are compared with the previously obtained experimental measurements and theoretical calculations for GaN [35, 36]. Peak positions of the hybridized peaks for all the samples are listed in Table 3. In NW, peaks related to hybridized N2p-Ga4p, N2p-Ga4s and its satellite shift to higher binding energy (B.E) to 4.1 eV, 6.1 eV and 8.1 eV, respectively, whereas satellite peak of Ga 3d shifts towards lower B.E to 9.6 eV. Additional peak at 11.4 eV corresponds to N2p-N2s-Ga3d hybridization. In s-NWN, N2p-Ga4p undergoes a higher B.E shift, whereas N2p-Ga4s along with its satellite and satellite of Ga 3d shifts to lower B.E. A peak at 10.4 eV corresponds to N2p-N2s-Ga3d hybridization. b-NWN consists of four peaks out of which N2p-Ga4p shifts to higher B.E and N2p-Ga4s shifts to lower B.E, whereas the remaining two satellite peak positions are unchanged, like in those of the epilayer.

Table 3 Peak positions for various hybridized levels as obtained from deconvoluted valence band spectra with shallow core levels of all the samples compared with those of epilayer

Hybridized peaks	Epilayer	NW	s-NWN	b-NWN
Ga 4p	–	–	–	–
N2p-Ga4p	4.0	4.1	4.5	4.1
N2p-Ga4s	6.0	6.1	5.9	5.9
Satellite peak	7.9	8.1	7.2	7.9
Satellite peak	9.8	9.6	8.6	9.8
N2p-N2s-Ga3d	–	11.4	10.4	–

Figure 7a shows a comparison of normalized intensities of hybridized peaks obtained by resolving the XPS valence band spectra (Fig. 6) for all the samples. In the epilayer, it is observed that the N2p-Ga4p hybridization is more dominant than the N2p-Ga4s hybridization, which is also observed for the MBE-grown NWN samples but is reversed in case of CVD-grown samples. This is a consequence of difference in the kinetics of growth and surface relaxation. Similarly, N2p-N2s-Ga3d peak is present for both NW and s-NWN samples, wherein for s-NWN it is much larger than the other two hybridized peaks.

It can be inferred from Fig. 7a that the nanostructures with smaller size (NW and s-NWN) tend to hybridize N2p-N2s-Ga3d levels which shifts the valence band spectra towards higher binding energy, due to a better charge transfer thereby in the formation of a more electronically relaxed structure. Whereas in b-NWN which contains larger nanostructures, the valence band shifts towards lower binding energy close to Fermi level. Figure 7b shows the plot of PL peak values vs the valence band maximum (VBM) values obtained from XPS for all the samples. The nature of plot linearly increases indicating that as the size of the nanostructures reduces, the VBM tends to shift away from Fermi level and consequently blue-shifting the PL emission.

Figure 8 shows schematic band diagram derived from XPS and PL data. It is clear from the Fig. 7 that smaller nanostructures (NW and s-NWN) exhibit a downward shift, whereas larger nanostructures (b-NWN) exhibit an upward shift in band structure compared to those in the epilayer. It is interesting to note that b-NWN exhibits higher band edge

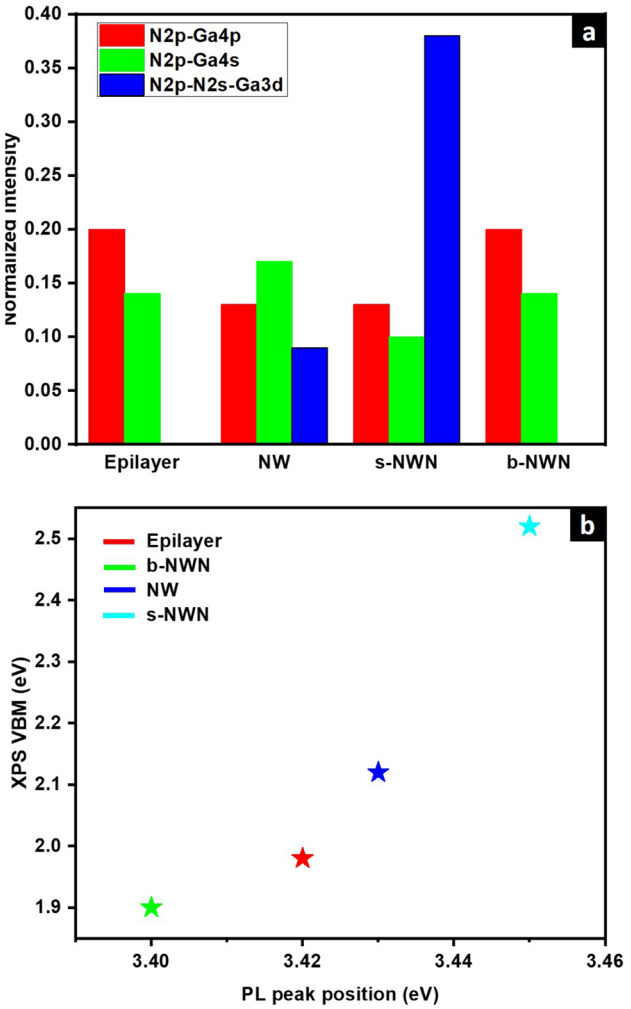

Fig. 7 **a** Comparative bar graph of normalized intensities of hybridized peaks (excluding satellite peaks) present in XPS valence band spectra for all the samples. **b** Plot of PL peak position vs the valence band maximum obtained from XPS for all the samples

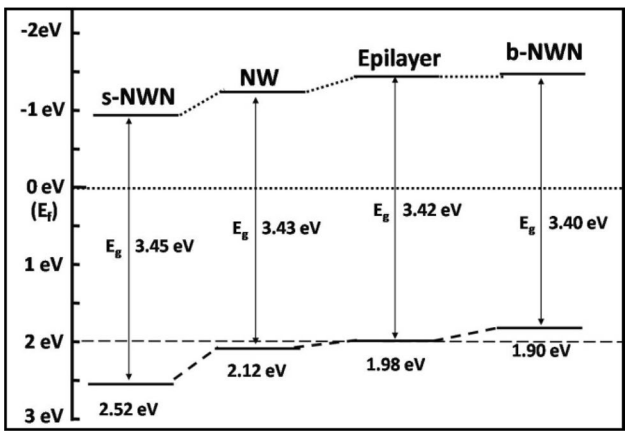

Fig. 8 Schematic band diagram derived from the data of XPS valence band and PL spectra

emission even though its bandgap is narrower compared to epilayer. As the size decreases, the VBM shifts away from Fermi level causing the widening of the bandgap and resulting in the red-shift in the BEE as observed in PL studies. The strain in MBE-grown nanowalls is majorly due to lattice mismatch between the sapphire substrate and overgrown GaN layer. Both nanowall morphologies exhibit compressive strain along the c-plane owing to the kinetics of their growth along *c*-direction. It has been widely noticed in the literature that nanowires of different aspect ratios and different materials do contain a small amount of strain [38–42]. Such strain may not be due to impurities or parasitic residues, but due to the nature of the inherent assembly during the growth via different kinetic routes. In light of this, we observe that there is a small tensile stress in the a–b plane of both the 1D configurations (NR and NW), and an additional tensile and compressive stress along *c*-direction in NW and NR, respectively. Due to the reduced influence of surface effects (free energy and surface reconstruction) in thicker rods, a compressive stress along *c*-direction is observed. However, in case of thinner nanowires due to the proximity of the surface, the unit cell along *c*-direction can get elongated resulting in the tensile stress. While the XRD and Raman studies indicate that the crystal strain-related properties are independent of size of nanostructures, PL and XPS studies exhibit a strong correlation between size and optical emission, as well as surface electronic structure.

4 Conclusions

Single-crystalline GaN nanostructures grown using MBE and CVD on Si and sapphire substrates have been studied for their structural, optical and surface properties. XRD and Raman studies reveal the presence of compressive strain on the NR (smaller aspect ratio ≈ 10) and tensile strain in NW (larger aspect ratio ≈ 236) with negligible hydrostatic strain. However, MBE-grown NWNs possess tensile strain with an additional hydrostatic strain component. Photoluminescence studies reveal a blue shift in the BEE as the size of nanostructures decreases which can be due to confinement effect. XPS studies reveal the shift in VBM away from the Fermi level and widening of bandgap as the size of nanostructure decreases. The hybridization of electronic shallow core levels increases as the size of nanostructures decreases, resulting in a more stable electronic structure. We have sketched the subtle variation in the electronic band structure of these kinetically differently formed nanostructures. More studies on growth-dependent nano-manifestations are underway on this technologically important material.

Acknowledgements The authors thank Prof. C. N. R. Rao for his support and encouragement. Two of the authors, KU and NA, thank Ashok

Shettar for the support and encouragement. KU thanks TEQIP, Ministry of Human Resources Department, India for the financial support. The authors acknowledge Vision Group on Science & Technology, Government of Karnataka, India for providing the necessary research facility for carrying out the research work, and the instruments procured under grant sanctioned, bearing GRD-242, GRD-441, GRD No. 185 and GRD No. 539.

Author contributions KU: Conceptualization, Data curation, Formal analysis, Investigation, Methodology, Writing—original draft, Writing—review & editing. NA: Conceptualization, Methodology, Supervision, Writing—review & editing. SMS: Conceptualization, Methodology, Supervision, Writing—review & editing.

Compliance with ethical standards

Conflict of interest The authors declare that they have no known competing financial interests or personal relationships that could have appeared to influence the work reported in this paper.

References

1. A.N. Kadam, M. Moniruzzaman, S.-W. Lee, Dual functional S-doped g-C_3N_4 pinhole porous nanosheets for selective fluorescence sensing of $Ag^+$and visible-light photocatalysis of dyes. Molecules **24**(3), 450 (2019)
2. B. Babua, J. Shima, A.N. Kadam, K. Yoo, Modification of porous g-C_3N_4 nanosheets for enhanced photocatalytic activity: in-situ synthesis and optimization of NH_4Cl quantity. Catal. Commun. **124**, 123–127 (2019)
3. L. Wang, T. Li, X. Long, X. Wang, Y. Xu, Y. Yao, Bimetallic catalytic growth of boron nitride nanotubes. Nanoscale **9**, 1816–1819 (2017)
4. D. Rasic, R. Sachan, M.F. Chisholm, J. Prater, J. Narayan, Room temperature growth of epitaxial titanium nitride films by pulsed laser deposition. Cryst. Growth Des. **17**(12), 6634–6640 (2017)
5. S. Nakamura, T. Mukai, M. Senoh, Candela-class high-brightness InGaN/AlGaN double-heterostructure blue-light-emitting diodes. Appl. Phys. Lett. **64**, 1687–1689 (1994)
6. M.F. Cansizoglu, S.M. Hamad, D.P. Norman, F. Keles, E. Badraddin, T. Karabacak, H.-W. Seo, PiN InGaN nanorod solar cells with high short-circuit current. Appl. Phys. Express **8**, 042302–042305 (2015)
7. X. Zhang, B. Liu, Q. Liu, W. Yang, C. Xiong, J. Li, X. Jiang, Ultrasensitive and highly selective photodetections of UV-A rays based on individual bicrystalline GaN nanowire. ACS Appl. Mater. Interfaces **9**, 2669–2677 (2017)
8. J. Anaya, H. Sun, J. Pomeroy, M. Kuball, Thermal management of GaN-on-diamond high electron mobility transistors: effect of the nanostructure in the diamond near nucleation region. 15th IEEE Intersociety Conference on Thermal and Thermomechanical Phenomena in Electronic Systems, 8 (2016) 332−343
9. D.P. Tran, M.A. Winter, B. Wolfrum, R. Stockmann, C.-T. Yang, M. Pourhassan-Moghaddam, A. Offenhäusser, B. Thierry, Toward intraoperative detection of disseminated tumor cells in lymph nodes with silicon nanowire field effect transistors. ACS Nano **10**, 2357–2364 (2016)
10. N. Jamond, P. Chrétien, L. Gatilova, E. Galopin, L. Travers, J.-C. Harmand, F. Glas, F. Houzé, N. Gogneau, Energy harvesting efficiency in GaN nanowire-based nanogenerators: the critical influence of the Schottky nanocontact. Nanoscale **9**, 4610–4619 (2017)
11. Q.N. Abdullah, F.K. Yam, J.J. Hassan, C.W. Chin, Z. Hassan, M. Bououdina, High performance room temperature GaNnanowires hydrogen gas sensor fabricated by chemical vapor deposition (CVD) technique. Int. J. Hydrogen Energy **38**, 14085–14101 (2013)
12. M. Peng, X. Zheng, Z. Ma, H. Chen, S. Liu, Y. He, M. Li, Ni-pattern guided GaN nanowire-array humidity sensor with high sensitivity enhanced by UV photoexcitation. Sens. Actuators B **256**, 367–373 (2018)
13. L.-W. Yin, Y. Bando, Y.-C. Zhu, D. Goldberg, L.-W. Yin, M.-S. Li, Indium-assisted synthesis on GaN nanotubes. Appl. Phys. Lett. **84**, 3912 (2004)
14. X. Xiang, C. Cao, Y. Xu, H. Zhu, Large-scale synthesis and optical properties of hexagonal GaN micropyramid/nanowire homostructures. Nanotechnology **17**, 30 (2006)
15. S.Y. Bae, H.W. Seo, J. Park, H. Yang, S.A. Song, Synthesis and structure of gallium nitride nanobelts. Chem. Phys. Lett. **365**, 525 (2002)
16. Z.J. Li, X.L. Chen, H.J. Li, Q.Y. Tu, Z. Yang, Y.P. Xu, B.Q. Hu, Synthesis and Raman scattering of GaN nanorings, nanoribbons and nanowires. Appl. Phys. A **72**, 629 (2001)
17. V. Venugopal, K. Upadhyaya, K. Kumar, S.M. Shivaprasad, Ion induced compositional changes and nanodroplet formation on GaN surface. Appl. Surf. Sci. **315**, 440–444 (2014)
18. S. Sharvani, K. Upadhayaya, G. Kumari, C. Narayana, S.M. Shivaprasad, Nano-morphology induced additional surface plasmon resonance enhancement of SERS sensitivity in Ag/GaN nanowall network. Nanotechnology **26**, 465701 (2015)
19. S. Wu, L. Wang, Z. Liu, X. Yi, Y. Huang, C. Yang, T. Wei, J. Yan, G. Yuan, J. Wang, J. Li, Ultrafast growth of horizontal GaN nanowires by HVPE through flipping the substrate. Nanoscale **10**, 5888–5896 (2018)
20. X. Zhang, S. Yang, C.G. Tu, Y.W. Kiang, C.C. Yang, Growth model of a GaN nanorod with the pulsed-growth technique of metalorganic chemical vapor deposition. Cryst. Growth Des. **8**(7), 3767–3773 (2018)
21. R. Sun, G.G. Wang, Z.C. Peng, Fabrication and UV photoresponse of GaN nanowire-film hybrid films on sapphire substrates by chemical vapor deposition method. Mater. Lett. **217**, 288–291 (2018)
22. A.K. Prasad, P.K. Sahoo, S. Dhara, S. Dash, A.K. Tyagi, Differences in hydrogen absorption over Pd and Pt functionalized CVD-grown GaN nanowires. Mater. Chem. Phys. **211**, 355–360 (2018)
23. P. Kumar, M. Tuteja, M. Kesaria, U.V. Waghmare, S.M. Shivaprasad, Superstructure of self-aligned hexagonal GaN nanorods formed on nitrided Si (111) surface. Appl. Phys. Lett. **101**, 131605 (2012)
24. V. Purushothaman, K. Jeganathan, Investigations on the role of Ni-catalyst for the VLS growth of quasi-aligned GaN nanowires by chemical vapor deposition. J. Nanopart. Res. **15**, 1789 (2013)
25. V. Purushothaman, K. Jeganathan, Structural evolution and growth mechanism of self-assembled wurtzite gallium nitride (GaN) nanostructures by chemical vapor deposition. J. Phys. Chem. C **117**(14), 7348–7357 (2013)
26. S.M. Roper, A.M. Anderson, S.H. Davis, P.W. Voorhees, Radius selection and droplet unpinning in vapor–liquid–solid-grown nanowires. J. Appl. Phys. **107**, 114320 (2010)
27. X. Weng, R.A. Burke, J.M. Redwing, The nature of catalyst particles and growth mechanisms of GaN nanowires grown by Ni-assisted metal–organic chemical vapor deposition. Nanotechnology **20**(8), 085610 (2009)
28. K. Upadhyaya, S. Sharvani, N. Ayachit, S.M. Shivaprasad, Charge transfer-induced enhancement of a Raman signal in a hybrid Ag–GaN nanostructure. RSC Adv. **9**(49), 28554–28560 (2019)
29. B.A. Wacaser, K.A. Dick, J. Johansson, M.T. Borgstrom, K. Deppert, L. Samuelson, Preferential interface nucleation: an expansion

of the VLS growth mechanism for nanowires. Adv. Mater. **21**, 153 (2008)
30. S. Kodambaka, J. Tersoff, M.C. Reuter, F.M. Ross, Diameter-independent kinetics in the vapor–liquid–solid growth of Si nanowires. Phys. Rev. Lett. **96**, 096105 (2006)
31. S. Shetty, M. Kesaria, J. Ghatak, S.M. Shivaprasad, The origin of shape, orientation, and structure of spontaneously formed wurtzite GaN nanorods on cubic Si (001) surface. Cryst. Growth Des. **13**(6), 2407–2412 (2013)
32. K. Upadhyaya, N. Ayachit, S.M. Shivaprasad, Stress induced modification of electronic band structure and enhanced optical emission in 1-D GaN nanostructures. Solid State Sci. **105**, 106242 (2020)
33. M. Kesaria, S.M. Shivaprasad, Nitrogen flux induced GaN nanostructure nucleation at misfit dislocations on Al_2O_3(0001). Appl. Phys. Lett. **99**(14), 143105 (2011)
34. M. Kesaria, S. Shetty, S.M. Shivaprasad, Evidence for dislocation induced spontaneous formation of GaN nanowalls and nanocolumns on bare C-plane sapphire. Cryst. Growth Des. **11**(11), 4900–4903 (2011)
35. V. Thakur, M. Kesaria, S.M. Shivaprasad, Enhanced band edge luminescence from stress and defect free GaN nanowall network morphology. Solid State Commun. **171**, 8–13 (2013)
36. V. Thakur, S.M. Shivaprasad, Electronic structure of GaN nanowall network analysed by XPS. Appl. Surf. Sci. **327**, 389–393 (2015)
37. M. Magnuson, M. Mattesini, C. Hoglund, J. Birch, L. Hultman, Electronic structure of GaN and Ga investigated by soft x-ray spectroscopy and first-principles methods. Phys. Rev. B **81**, 085125 (2010)
38. H.W. Seo, S.Y. Bae, J. Park, H. Yang, K.S. Park, S. Kim, Strained gallium nitride nanowires. J. Chem. Phys. **116**(21), 9492 (2002)
39. B.M. Ming, R.Z. Wang, C.Y. Yam, L.C. Xu, W.M. Lau, H. Yan, Bandgap engineering of GaN nanowires. AIP Adv. **6**(5), 055018 (2016)
40. S.D. Dabhi, P.K. Jha, Ab initio study of strained wurtzite InAs nanowires: engineering an indirect–direct band gap transition through size and uniaxial strain. RSC Adv. **5**(109), 89993 (2015)
41. L. Huang, S. Lu, P. Chang, K. Banerjee, R. Hellwarth, J.G. Lu, Structural and optical verification of residual strain effect in single crystalline CdTe nanowires. Nano Res. **7**(2), 228 (2013)
42. J. Loh, D. Baillargeat (2013) Strain-induced phononic and structural response in wurtzite-gallium nitride nanowires. MRS Proceedings 1548, mrss13-1548-n05-03.